ADVANCED FUNCTIONAL MATERIALS
www.afm-journal.de

Materials Views
www.MaterialsViews.com

Improved Photocatalytic Performance of Heterojunction by Controlling the Contact Facet: High Electron Transfer Capacity between TiO_2 and the {110} Facet of $BiVO_4$ Caused by Suitable Energy Band Alignment

Houfen Li, Hongtao Yu, Xie Quan, Shuo Chen, and Huimin Zhao*

Charge separation at the interface of heterojunctions is affected by the energy band alignments of the materials that compose the heterojunctions. Controlling the contact crystal facets can lead to different energy band alignments owing to the varied electronic structures of the different crystal facets. Therefore, $BiVO_4$-TiO_2 heterojunctions are designed with different $BiVO_4$ crystal facets at the interface ({110} facet or {010} facet), named $BiVO_4$-110-TiO_2 and $BiVO_4$-010-TiO_2, respectively, to achieve high photocatalytic performance. Higher photocurrent density and lower photoluminescence intensity are observed with the $BiVO_4$-110-TiO_2 heterojunction than those of the $BiVO_4$-010-TiO_2 heterojunction, which confirms that the former possesses higher charge carrier separation capacity than the latter. The photocatalytic degradation results of both Rhodamine B and 4-nonylphenol demonstrate that better photocatalytic performance is achieved on the $BiVO_4$-110-TiO_2 heterojunction than the $BiVO_4$-010-TiO_2 heterojunction under visible light (≥422 nm) irradiation. The higher electron transfer capacity and better photocatalytic performance of the $BiVO_4$-110-TiO_2 heterojunction are attributed to the more fluent electron transfer from the {110} facet of $BiVO_4$ to TiO_2 caused by the smaller interfacial energy barrier. This is further confirmed by the selective deposition of Pt on the TiO_2 surface as well as the longer lifetime of Bi^{5+} in the $BiVO_4$-110-TiO_2 heterojunction.

1. Introduction

Heterojunction construction is an effective approach to improve the photocatalytic performance of photocatalysts.[1–5] With light irradiation, electrons and holes in the heterojunction move in opposite directions under the driving of a built-in electric field. The charge carriers are thus separated and the carrier lifetime is prolonged.[4,5] As well-matched energy band alignment is a key factor for the achievement of efficient heterojunctions,[6,7] various energy band engineering methods, such as crystalline phase optimization,[8,9] adjustion of element proportions in the compound,[10] element doping,[9] and insertion of interlayers,[11] have been explored to modulate the energy band levels of component materials in heterojunctions. Furthermore, recent work has confirmed that different crystal facets of even the same crystalline phase are endowed with various energy band levels owing to the varied surface electronic structures associated with them.[12–15] In this regard, a lack of control over the interfacial contact facets would lead to the presence of heterojunctions with various energy band alignments. This is of intense effect in charge carrier migration in formed heterojunctions, which has been one of the reasons for the limited success for further improvements of heterojunction performance. For example, Wang and co-workers proved that the {111} facet of Cu_2O, with a lower work function than the {100} facet, is unfavorable for the migration of holes from the Cu_2O surface to Pd through a semiconductor-metal junction.[15,16] Hence, it is imperative to select and control the contact facet in a heterojunction for the acquisition of suitable energy band levels and the consequent excellent charge separation performance. However, to the best of our knowledge, very limited attention has been paid to either the preparation methods or the performance study of heterojunctions contacted by different crystal facets.

A typical example of a semiconductor with different energy band structures on different facets is monoclinic bismuth vanadate (m-$BiVO_4$), a promising visible light photocatalyst with a direct band gap of ≈2.4 eV.[17–19] Recent studies confirmed that the conduction band edge and valence band edge of the {110} facet of m-$BiVO_4$ are higher by 0.42 and 0.37 eV, respectively, than those of its {010} facet.[20] The individual energy band levels for separate facets of $BiVO_4$ have led to different behaviors of the {110} facet and {010} facet in the photocatalytic process, with oxidation and reduction reactions occurring separately on each facet, respectively. Given the above facts, different energy band levels[20–22] of the separate facets of $BiVO_4$ are considered to play key roles in affecting the performance

Dr. H. Li, Assoc. Prof. H. Yu, Prof. X. Quan, Assoc. Prof. S. Chen, Prof. H. Zhao
Key Laboratory of Industrial Ecology and Environmental Engineering (Ministry of Education)
School of Environmental Science and Technology
Dalian University of Technology
Dalian 116024, China
E-mail: quanxie@dlut.edu.cn

DOI: 10.1002/adfm.201500521

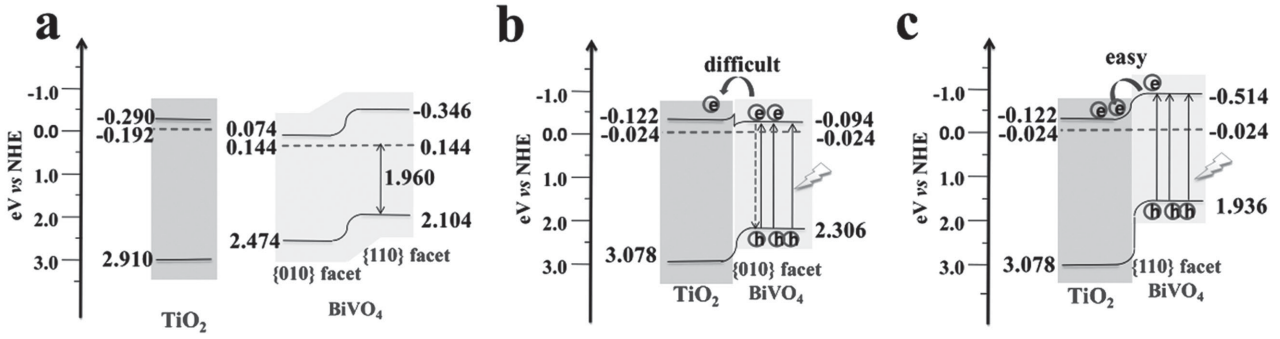

Scheme 1. Relative energy band levels of TiO_2, $BiVO_4$ {010} facet, $BiVO_4$ {110} facet, and two kinds of $BiVO_4$-TiO_2 heterojunctions by different contact facets.

of heterojunctions with other materials. For instance, some researchers stated the m-$BiVO_4$-TiO_2 heterojunction exhibited an improved photocatalytic efficiency,[8,23] while another study reported that the relative conduction and valence band positions of m-$BiVO_4$ and TiO_2 were unfavorable, which limited the charge separation efficiency of the heterojunction.[9] The different behaviors may be related to the different contact facets between the materials.

Herein, taking $BiVO_4$ and TiO_2 as a proof-of-concept, we first designed two types of $BiVO_4$-TiO_2 heterojunctions by selectively growing TiO_2 on the {110} facet and {010} facet of $BiVO_4$, respectively, with or without TiO_2 seeding prior to the hydrothermal process. In this research, the binding energy of the onset edge (E_{vf}) and the Fermi level (E_f) of $BiVO_4$ are 1.96 eV versus NHE and 0.144 eV versus NHE, respectively, determined by the valence band X-ray photoelectron spectroscopy and the Mott–Schottky plots (Figure S1, Supporting Information). Therefore, the valence band maximum of the as-prepared $BiVO_4$ is 2.104 eV versus NHE, implying the top of the valence band of the {110} facet is 2.104 eV versus NHE. According to the energy band offset between the {010} facet and {110} facet, as well as the reported energy band level of TiO_2,[24,25] the energy band positions of the $BiVO_4$ {010} facet and $BiVO_4$ {110} facet, with respect to that of TiO_2, are illustrated in **Scheme 1**a. As a result, the energy band positions after forming $BiVO_4$-TiO_2 heterojunctions are represented in Scheme 1b,c. Compared with the {110} facet-TiO_2 interface, the {010} facet-TiO_2 exhibits a higher interfacial energy barrier between the conduction band of the {010} facet with that of TiO_2, which makes it more difficult for electrons of $BiVO_4$ to transfer to the conduction band of TiO_2. On the other hand, the heterojunction with TiO_2 grown on the {110} facet of $BiVO_4$ promises a higher charge carrier separation efficiency and higher photocatalytic performance than those of the heterojunction with TiO_2 grown on the {010} facet of $BiVO_4$, which is confirmed by the detailed tests in this study.

2. Results and Discussion

The scanning electron microscopy (SEM) image of the as-prepared $BiVO_4$ (Figure S2, Supporting Information) shows the regularly shaped sample of truncated bipyramid with exposed {010} and {110} facets was synthesized. Two kinds of $BiVO_4$-TiO_2 heterojunctions with TiO_2 grown on different facets of $BiVO_4$ were prepared following the process represented schematically in **Scheme 2**. **Figure 1**a,b and Figure S3a, Supporting Information, show the SEM images of the heterojunction with TiO_2 grown on the {010} facet of $BiVO_4$ (named $BiVO_4$-010-TiO_2). It reveals that the TiO_2 crystals were selectively

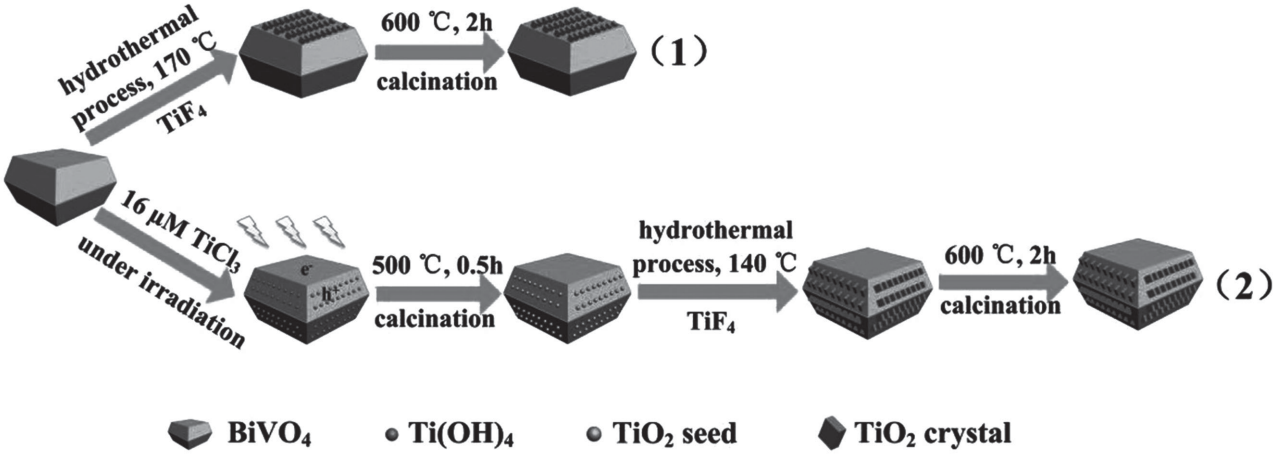

Scheme 2. Schematic illustration of the process to prepare $BiVO_4$-010-TiO_2 heterojunction (1) and $BiVO_4$-110-TiO_2 heterojunction (2).

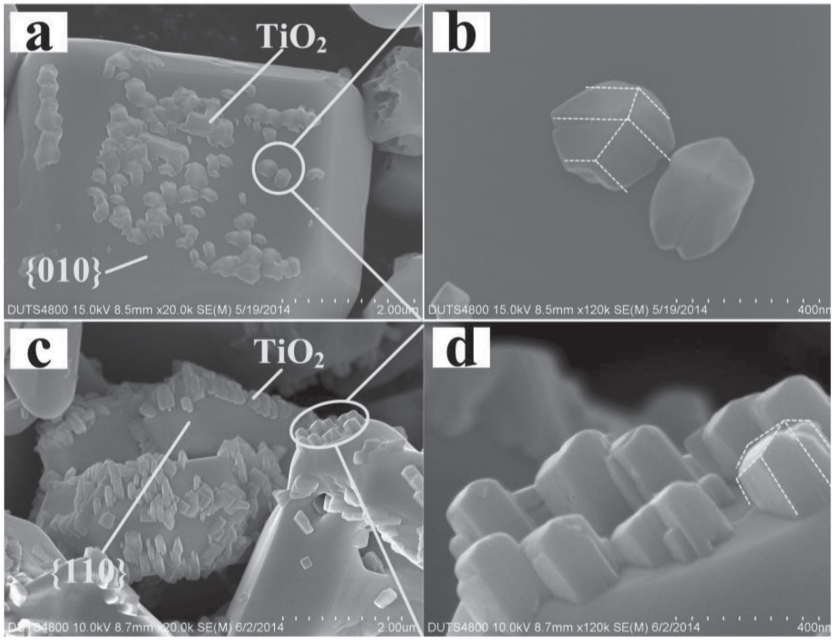

Figure 1. SEM images of $BiVO_4$-TiO_2 heterojunctions: a) $BiVO_4$-010-TiO_2 heterojunction and b) TiO_2 grown on the {010} facet of $BiVO_4$ (TiO_2 was grown with HF aqueous solution containing TiF_4 precursor in the presence of $BiVO_4$ at 170 °C for 12 h); c) $BiVO_4$-110-TiO_2 heterojunction and d) TiO_2 grown on the {110} facet of $BiVO_4$ (TiO_2 was grown with HF aqueous solution containing TiF_4 precursor in the presence of TiO_2 seeded $BiVO_4$ at 140 °C for 12 h).

grown on the {010} facet of $BiVO_4$ during the hydrothermal process at 170 °C using TiF_4 as precursor. Its preferential growth on the {010} facet is ascribed to the two low coordinated oxygen atoms and O with a dangling bond in VO_4^{3-}, which could provide sufficient binding sites to anchor Ti^{4+}.[22] On the other hand, the small *d*-value mismatch (≤10%) between TiO_2 and the {010} facet of $BiVO_4$ is speculated to account for the preferential nucleation of TiO_2 on the {010} facet,[26] while the larger d-value mismatch between TiO_2 and the {110} facet of $BiVO_4$ hampered the nucleation of TiO_2 on the {110} facet of $BiVO_4$. For achievement of the heterojunction with TiO_2 grown on the {110} facet of $BiVO_4$ (named $BiVO_4$-110-TiO_2), a seeding process of TiO_2 was first conducted, by oxidizing Ti^{3+} to Ti^{4+} selectively on the {110} facet of $BiVO_4$ followed by 30 min calcination at 500 °C for the formation of TiO_2 seeds. The seeding process occurs on the {110} facet but is absent from the {010} facet, which is inherently related to their different roles under light irradiation: the {110} facet of $BiVO_4$ acts as an oxidation site and the {010} facet as a reduction site.[20] The TiO_2 seeds on the {110} facet of $BiVO_4$ were grown under a low-temperature hydrothermal process at 140 °C to a comparative size to those on the {010} facet, for sizes of ≈200–300 nm (Figure 1c,d and Figure S3b, Supporting Information). It is worth mentioning that no TiO_2 appeared when the seeding process was skipped during the preparation process for $BiVO_4$-110-TiO_2 heterojunction, which prevented the growth of TiO_2 on the {010} facet for the $BiVO_4$-110-TiO_2 heterojunction.

The surface atomic composition and the chemical state of the heterojunctions were investigated using X-ray photoelectron spectroscopy (XPS). **Figure 2**a presents the survey spectra of the $BiVO_4$ sample, the $BiVO_4$-010-TiO_2 heterojunction and $BiVO_4$-110-TiO_2 heterojunction, from which only elements of Bi, V, Ti, and O were obtained, indicating other elements during the preparation process had been removed after washing and the calcining process. From the high-resolution XPS spectra of elemental Ti in Figure 2b,c, it can be clearly recognized that the binding energy of elemental Ti is 458.1 eV for both $BiVO_4$-110-TiO_2 and $BiVO_4$-010-TiO_2 heterojunctions, in good agreement with that of Ti(IV).[27] From this result, it can be deduced that the Ti^{3+} during the seeding process had been successfully oxidized to Ti^{4+}, and all the elemental Ti existed in the form of TiO_2 on both the {010} facet and {110} facet of $BiVO_4$. By adjusting the content of the TiF_4 precursor, a very similar TiO_2 content was obtained for $BiVO_4$-110-TiO_2 heterojunction (Ti/Bi = 4.42%) as was obtained for $BiVO_4$-010-TiO_2 heterojunction (Ti/Bi = 4.61%), which avoids the effect of TiO_2 content on charge carrier separation capacities of the two kinds of heterojunctions.

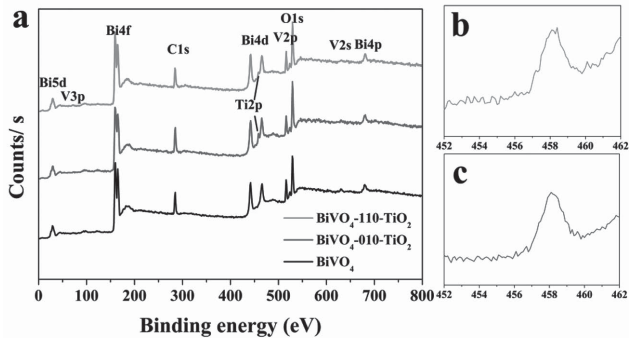

Figure 2. X-ray photoelectron spectra: a) survey spectra; high resolution spectra of elemental Ti in two kinds of $BiVO_4$-TiO_2 heterojunctions: b) $BiVO_4$-110-TiO_2 heterojunction and c) $BiVO_4$-010-TiO_2 heterojunction.

X-ray diffraction (XRD) patterns in **Figure 3** revealed that monoclinic $BiVO_4$ was successfully synthesized, with obvious peaks assigned to the {110} facet ($2\theta = 18.67°$ and 18.99°) and a peak belonging to the {010} facet ($2\theta = 30.55°$) (PDF#14-0688). The agreement of $BiVO_4$-TiO_2 heterojunction patterns with those of $BiVO_4$ indicates the introduction of TiO_2 did not change the crystal phase and crystallinity of $BiVO_4$. However, no diffraction peaks corresponding to TiO_2 were observed in the XRD patterns of either $BiVO_4$-010-TiO_2 or $BiVO_4$-110-TiO_2 heterojunctions, which was proposed to arise from the low TiO_2 content. As an alternative approach for the determination of the TiO_2 crystalline phase, the selected-area electron diffraction (SAED) patterns of the TiO_2 on both heterojunctions were obtained (Figure S4, Supporting Information). The acquired lattice spacings as well as the interfacial angles of $BiVO_4$-010-TiO_2 heterojunction agreed well with (200) and (107) facets of anatase TiO_2, and those for $BiVO_4$-110-TiO_2 heterojunction

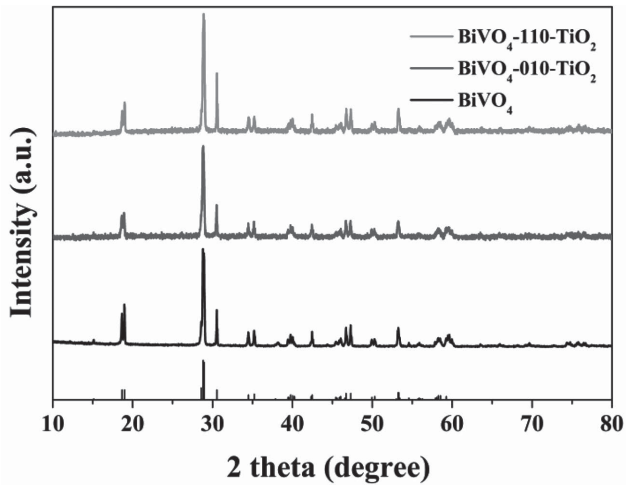

Figure 3. XRD patterns of $BiVO_4$, $BiVO_4$-010-TiO_2 heterojunction and $BiVO_4$-110-TiO_2 heterojunction.

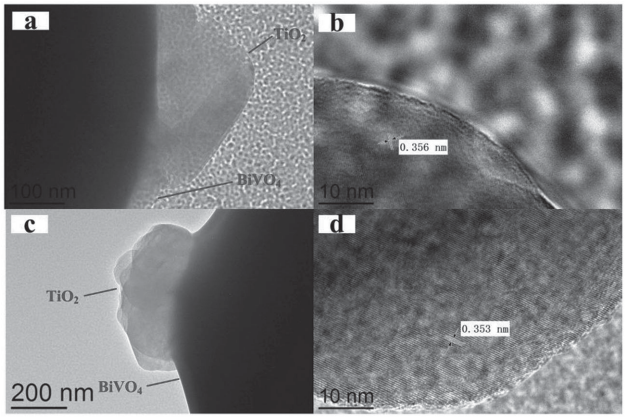

Figure 4. TEM images of $BiVO_4$-TiO_2 heterojunctions: a,b) $BiVO_4$-010-TiO_2 heterojunction and c,d) $BiVO_4$-110-TiO_2 heterojunction.

accord with some other atomic planes of anatase TiO_2 ((112) and (004) facets), which demonstrated TiO_2 on both heterojunctions were in this crystal phase. The images of high-resolution transmission electron microscopy (HRTEM) showed that the lattice spacing values of 0.356 nm (**Figure 4**a,b) for TiO_2 of the $BiVO_4$-010-TiO_2 heterojunction and 0.353 nm (Figure 4c,d) for TiO_2 of the $BiVO_4$-110-TiO_2 heterojunction are very close to that of the anatase {101} crystallographic plane (0.352 nm, PDF#21-1272). This suggested that TiO_2 on both heterojunctions exposed with similar facets of the anatase crystal phase, and the frames of TiO_2 crystals were traced out in Figure 1b,d to make the orientation of TiO_2 more distinguishable. The consistency of the TiO_2 crystal phase and exposed facets ensures the same energy band levels of TiO_2 at the two kinds of crystal facets, guaranteeing the absence of TiO_2 energy band-level variation.

The band gap energy of $BiVO_4$ was calculated to be 2.4 eV according to its ultraviolet–visible diffuse reflectance spectrum (DRS) (Figure S5a, Supporting Information), and the DRS spectra of $BiVO_4$-TiO_2 heterojunctions illustrated that the incorporation of anatase TiO_2 did not change the light absorption property of $BiVO_4$ (Figure S5b, Supporting Information). Despite the same light-harvesting capacities, the $BiVO_4$-TiO_2 heterojunctions showed enhanced charge carrier separation efficiency, which was determined from the photocurrent densities as well as the photoluminescence (PL) spectra. From **Figure 5**a, it can be seen that with only $BiVO_4$ optically excited by adopting a long-pass filter (≥422 nm), $BiVO_4$-TiO_2 heterojunctions exhibited improved photocurrent densities compared with pure $BiVO_4$ owing to the enhanced photogenerated charge carrier separation performance at the interface. More importantly, the $BiVO_4$-110-TiO_2 heterojunction displayed an even higher photocurrent density than that of the $BiVO_4$-010-TiO_2 heterojunction, with values of 0.18 and 0.14 μA cm^{-2}, respectively. This phenomenon indicated that the photogenerated charge carriers of the $BiVO_4$-110-TiO_2 heterojunction enjoyed an even higher separation efficiency, which is in accord with the findings from the energy band alignment. Moreover, the PL spectra were in agreement with the above results, with the highest photoluminescence intensity observed for $BiVO_4$ (Figure 5b), indicating its high photogenerated electron–hole recombination efficiency, and the lowest photoluminescence intensity observed for the $BiVO_4$-110-TiO_2 heterojunction, which was attributed to the most suppressed electron-hole recombination process. The two kinds of heterojunctions exhibited a greater behavior difference for the photoluminescence intensities than that of photocurrent densities. That is because the 330-nm excitation wavelength, used to obtain the PL spectra, excited TiO_2 at the same time. Under this condition, photogenerated holes in TiO_2 transfer to $BiVO_4$ and accelerate the electron–hole recombination in the case of the $BiVO_4$-010-TiO_2 heterojunction. Both the results of photocurrent density and photoluminescence tests clarified that the $BiVO_4$-110-TiO_2 heterojunction with TiO_2 on the {110} facet of $BiVO_4$ exhibited better charge separation performance than that of $BiVO_4$-010-TiO_2 for the same material and content.

As one typical pollutant model for evaluation of the photocatalytic performance of $BiVO_4$, an organic dye, namely, Rhodamine B (RhB), was employed to study the photocatalytic activities of $BiVO_4$-TiO_2 heterojunctions under visible light irradiation. From **Figure 6**a, it can be observed that the concentration

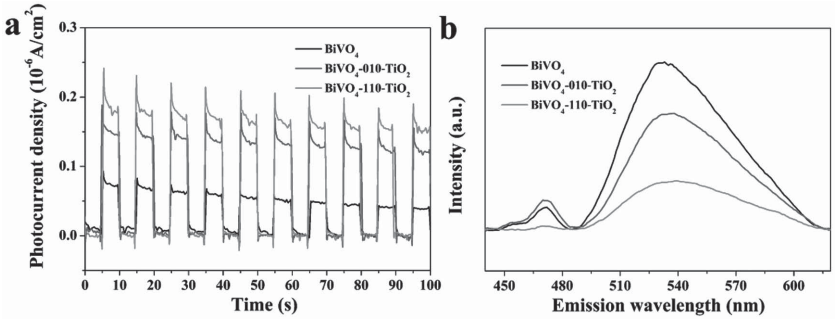

Figure 5. a) Photocurrent density–time curves of $BiVO_4$, $BiVO_4$-010-TiO_2 heterojunction and $BiVO_4$-110-TiO_2 heterojunction (bias: 0 V vs SCE, 0.1 M Na_2SO_4, light irradiation: ≥422 nm, 100 mW cm^{-2}); b) PL spectra of $BiVO_4$, $BiVO_4$-010-TiO_2 heterojunction and $BiVO_4$-110-TiO_2 heterojunction, with excitation wavelength of 330 nm.

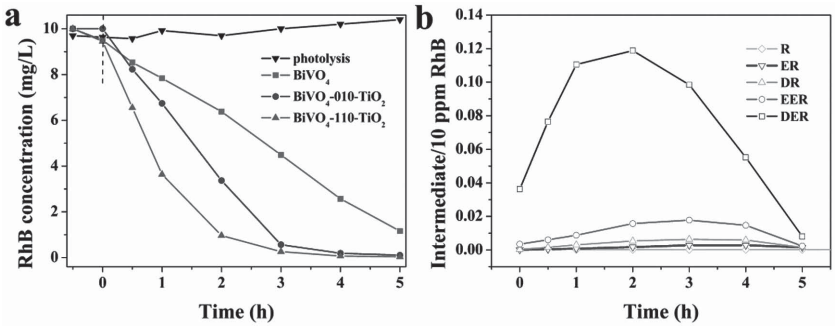

Figure 6. a) concentration of RhB versus time plotted for $BiVO_4$ and $BiVO_4$-TiO_2 heterojunctions under visible light irradiation and b) intermediates of RhB degradation during the photocatalytic process in panel a with $BiVO_4$-110-TiO_2 heterojunction (light irradiation: ≥422 nm, 100 mW cm^{-2}).

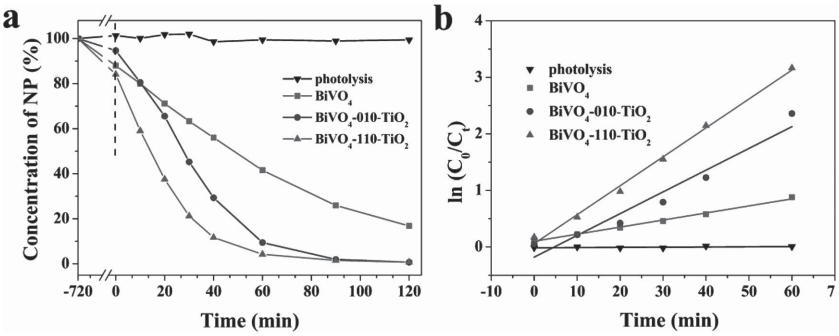

Figure 7. a) Percent concentration of 4-nonylphenol versus time for $BiVO_4$-TiO_2 heterojunctions under visible light irradiation (initial concentration: 1×10^{-4} M, light irradiation: ≥422 nm, 100 mW cm^{-2}) and b) the kinetics of photocatalytic degradation of 4-nonylphenol in panel (a).

of RhB exhibited almost no change without $BiVO_4$ or $BiVO_4$-TiO_2 heterojunction photocatalysts, indicating it was stable under visible light irradiation. It is obvious that RhB degraded faster in the presence of $BiVO_4$-TiO_2 heterojunctions than in the presence of the $BiVO_4$ photocatalyst, which arose from the enhanced photogenerated charge carrier separation capacities of $BiVO_4$ in heterojunctions. Furthermore, $BiVO_4$-110-TiO_2 heterojunction displayed an even higher kinetic rate constant (1.19 h^{-1}) than that of $BiVO_4$-010-TiO_2 heterojunction (0.98 h^{-1}) over the duration of the experiment. The outstanding photocatalytic performance of $BiVO_4$-110-TiO_2 heterojunction can be attributed to its higher charge carrier separation capacity compared with that of $BiVO_4$-010-TiO_2 heterojunction, which is supported by the results from the photocurrent density and photoluminescence tests. The intermediates of RhB during the photodegradation on $BiVO_4$-110-TiO_2 were monitored and the results are illustrated in Figure 6b and Figure S6, Supporting Information. As we can see, five intermediates, namely, *N*,*N*-diethyl-*N*′-ethylrhodamine (DER), *N*,*N*-diethylrhodamine (DR), *N*-ethyl-*N*′-ethylrhodamine (EER), *N*-ethylrhodamine (ER), and Rhodamine (R), were observed during this process. Their concentrations increased with prolonged irradiation and then decreased with longer time. The main intermediate, DER, reached its maximum at 2 h, whereas the maximum of the other intermediates was observed at 3 h. These results indicated that RhB was de-ethylated in a stepwise manner and further degraded completely on the $BiVO_4$-110-TiO_2 heterojunction.[28]

To eliminate the sensitization effect of RhB molecules during the visible light photocatalytic process, 4-nonylphenol was selected as another model contaminant to further evaluate the photocatalytic activity of $BiVO_4$-TiO_2 heterojunctions. The results are shown in **Figure 7**a,b. The blank test confirmed the photolysis of 4-nonylphenol was negligible, and the kinetic constant for photocatalytic degradation of 4-nonylphenol on pure $BiVO_4$ under visible light illumination was 0.75 h^{-1}. In agreement with the result obtained for the RhB degradation process, the $BiVO_4$-110-TiO_2 heterojunction exhibited the best photocatalytic activity for degradation of 4-nonylphenol, with the corresponding rate constant of 3.07 h^{-1} under visible light irradiation. By contrast, the photocatalytic kinetic constant for degradation of 4-nonylphenol over $BiVO_4$-010-TiO_2 heterojunction was 2.31 h^{-1} during ≈60 min of experiment under visible light irradiation. Therefore, the derived degradation rate on the $BiVO_4$-110-TiO_2 heterojunction was 4.09 and 1.33 times higher than those on $BiVO_4$ and the $BiVO_4$-010-TiO_2 heterojunction, respectively. This result further confirmed that the $BiVO_4$-110-TiO_2 heterojunction kept a higher charge carrier separation efficiency than that of the $BiVO_4$-010-TiO_2 heterojunction, which enabled the higher photocatalytic performance. This difference was proposed to originate from the aforementioned interfacial energy barrier difference. The smaller energy barrier of the $BiVO_4$-110-TiO_2 heterojunction promised more photoinduced electrons from $BiVO_4$ {110} facet transfer to TiO_2 and separate with holes on $BiVO_4$ during the photocatalytic process, contributing to its higher charge carrier separation efficiency and the consequent higher photocatalytic efficiency.

To verify the electron transfer behaviors between {010}/{110} facet and TiO_2, photodeposition of Pt under visible light irradiation (≥422 nm) was carried out using H_2PtCl_6 as the precursor and ethanol as a hole scavenger. SEM images (**Figure 8**a) clearly show that, in the case of the $BiVO_4$-110-TiO_2 heterojunction, particles of Pt were deposited on the TiO_2 surface but not

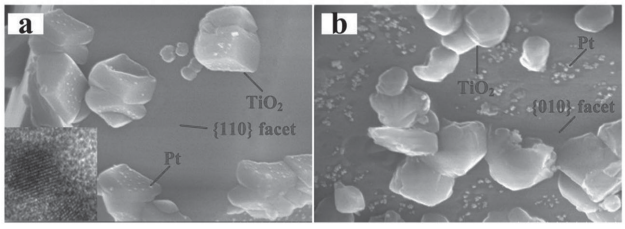

Figure 8. Photoreduction deposition of Pt on a) $BiVO_4$-110-TiO_2 heterojunction and b) $BiVO_4$-010-TiO_2 heterojunction under visible light irradiation (≥422 nm), the inset image in panel a is the lattice spacing of Pt on TiO_2 surface by HRTEM.

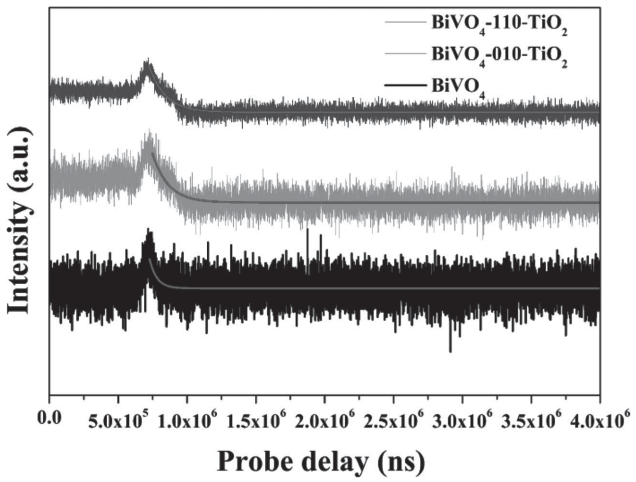

Figure 9. Transient absorption signal as a function of probe delay for $BiVO_4$, $BiVO_4$-010-TiO_2 heterojunction and $BiVO_4$-110-TiO_2 heterojunction (probed at 500 nm according to the optical absorption region).

the {110} facet of $BiVO_4$. However, for the $BiVO_4$-010-TiO_2 sample, Pt particles were prone to deposit on the {010} facet of $BiVO_4$ instead of the TiO_2 surface (Figure 8b). These findings corroborate the result that electron transfer to the TiO_2 surface occurred easier from the {110} facet than from the {010} facet. Further evidence was provided by the transient absorption spectra of $BiVO_4$, $BiVO_4$-010-TiO_2 and $BiVO_4$-110-TiO_2 heterojunctions shown in **Figure 9**. The decay signals of the photoexcited holes in $BiVO_4$[29] (intermediate species Bi^{5+} herein) were probed at 500 nm, and the lifetimes of the intermediate species Bi^{5+} were estimated to be 50, 115.86, and 120 µs for $BiVO_4$, $BiVO_4$-010-TiO_2 heterojunction and $BiVO_4$-110-TiO_2 heterojunction, respectively. The longest lifetime indicated the largest amount of Bi^{5+} produced in the $BiVO_4$-110-TiO_2 heterojunction,[30,31] which confirmed that more electrons were transferred to TiO_2 from the $BiVO_4$-110-TiO_2 heterojunction than from the $BiVO_4$-010-TiO_2 heterojunction. The higher possibility for electrons moving from the conduction band of the $BiVO_4$ {110} facet to the conduction band of TiO_2 is in accord with the prediction from the energy band structures. The lower potential barrier height between the {110} facet of $BiVO_4$ and TiO_2, compared with that between the {010} facet and TiO_2, leads to a more fluent electron transfer and contributes to the higher photocatalytic performance.

3. Conclusion

By controlling the seeding and growth processes of TiO_2 nanoparticles, $BiVO_4$-TiO_2 heterojunctions with different interfacial contact facets were obtained successfully. The experimental results demonstrated that the $BiVO_4$-110-TiO_2 heterojunction possesses better charge separation property and higher photocatalytic performance than that of $BiVO_4$-010-TiO_2 heterojunction. The selective photoreduction of Pt on the TiO_2 surface and the longer lifetime of Bi^{5+} for the $BiVO_4$-110-TiO_2 heterojunction than that of $BiVO_4$-010-TiO_2 heterojunction proved the superior performance of the former is attributed to the more fluent electron transfer to TiO_2 from the {110} facet of $BiVO_4$ than from the {010} facet of $BiVO_4$, which is caused by the suitable energy band alignment. These findings provide new avenues to understand and realize rationally designed heterojunctions with specified crystal facets, which is of importance to the enhancement of charge separation in heterojunctions and the resulting improved photocatalytic performance.

4. Experimental Section

Synthesis of $BiVO_4$-TiO_2 Heterojunctions: $BiVO_4$ was synthesized by a hydrothermal process according to previously published procedures,[20,32] and a schematic diagram for the preparation of $BiVO_4$-TiO_2 heterojunctions is given in Scheme 2. In a typical synthesis route for the $BiVO_4$-010-TiO_2 heterojunction, TiF_4 powder (0.025 g, 8×10^{-3} M) was dissolved in deionized water (25 mL, pH was adjusted to 2.0 with hydrochloric acid) in the presence of $BiVO_4$ (0.320 g), to which HF (50 µL, 40% w/w) was added. The mixture was transferred to a Teflon-lined autoclave and heated at 170 °C for 12 h. For the preparation of the $BiVO_4$-110-TiO_2 heterojunction, TiO_2 was first seeded on the {110} facet of $BiVO_4$ as follows: $BiVO_4$ powder was dispersed in $TiCl_3$ aqueous solution (16×10^{-6} M) under light irradiation; because of the unique oxidation property of the {110} facet, Ti^{3+} was oxidized to Ti^{4+} selectively on the {110} facet rather than the {010} facet of $BiVO_4$. This process was followed by thorough rinsing and calcination at 500 °C for 0.5 h, which led to the formation of TiO_2 seeds. The TiO_2 crystals were then grown following the same process as that of the $BiVO_4$-010-TiO_2 heterojunction, but a lower temperature of 140 °C was used for the hydrothermal process. After reaction, both products were washed several times with deionized water and dried at 60 °C, then were heated at 600 °C in a static air atmosphere in a furnace for 90 min to remove impurity elements.

Characterization: The crystal structures were investigated using an X-ray diffractometer (XRD, EMPYREAN, PANalytical), and the element states of the samples were analyzed by an X-ray photoelectron spectrometer (XPS, VG ESCALAB250) with Al-Kα irradiation (1486.6 eV). The morphologies of the $BiVO_4$-TiO_2 heterojunctions were observed using an S-4800 field emission scanning electron microscope (SEM, Hitachi Co., Japan), and the crystal structures of TiO_2 were distinguished by transmission electron microscopy (TEM) and the selected-area electron diffraction (SAED) patterns on a Tecnai G2 F30 S-Twin (FEICompany, USA). Ultraviolet–visible diffuse reflectance spectra (DRS) were recorded on a Shimadzu UV-2450 spectrophotometer. Photoluminescence (PL) spectra of the samples were measured using a fluorescence spectrometer (Hitachi F-4500). The nanosecond transient absorption data were recorded on a nanosecond laser flash photolysis spectrometer (LP920, Edinburgh Instruments Ltd., UK). The Mott–Schottky plots were measured in Na_2SO_4 electrolyte (0.1 M) at a frequency of 1 kHz using the electrochemical station (CHI660D, Shanghai Chenhua Limited, China) in a conventional three-electrode configuration.

Photocatalytic Reactions: Photocatalytic degradation processes of RhB and 4-nonylphenol on $BiVO_4$-010-TiO_2 heterojunction and $BiVO_4$-110-TiO_2 heterojunction were performed to evaluate their photocatalytic capabilities. A high-pressure xenon short arc lamp (CHF-XM35-500W, Beijing Changtuo Co.) was used as a light source with a visible light cut-off filter (≥422 nm). The light intensity was 100 mW cm^{-2} measured by a digital radiometer (FZ-A, Photoelectric Instrument Factory, Beijing Normal University). Before the photocatalytic process, 60 mg photocatalyst was added to a 20 mL RhB solution (10 mg L^{-1}) and the mixture was stirred in the dark for 30 min to ensure adsorption equilibrium. The RhB concentration and its intermediates during the process were determined by high-performance liquid chromatography (Waters 2695, USA) equipped with a photodiode array detector (Waters 2996). The 4-nonylphenol degradation test was carried out under the same light irradiation, with 30 mg photocatalyst added to the 20 mL

solution (1×10^{-4} M), and the mixture was stirred in the dark overnight to ensure adsorption equilibrium. The 4-nonylphenol concentration was determined by high-performance liquid chromatography with a multi-wavelength fluorescence detector (Waters 2475). The mobile phase was acetonitrile/water containing 0.1% trifluoroacetic acid at a flow rate of 1.0 cm^3 min^{-1}, and the excitation and detection wavelengths were set at 270 and 320 nm, respectively.[33]

Supporting Information

Supporting Information is available from the Wiley Online Library or from the author.

Acknowledgements

This work was financially supported by National Basic Research Program of China (2011CB936002) and National Natural Science Foundation of China (NSFC-JST 21261140334).

Received: February 6, 2015
Revised: March 16, 2015
Published online: April 7, 2015

[1] X. D. Fu, M. Z. Xie, P. Luan, L. Q. Jing, *ACS Appl. Mater. Interfaces* **2014**, *6*, 18550.
[2] Y. Hou, F. Zuo, A. Dagg, P. Feng, *Nano Lett.* **2012**, *12*, 6464.
[3] Y. Peng, M. Yan, Q.-G. Chen, C.-M. Fan, H.-Y. Zhou, A.-W. Xu, *J. Mater. Chem. A* **2014**, *2*, 8517.
[4] H. T. Yu, X. Quan, S. Chen, H. M. Zhao, *J. Phys. Chem. C* **2007**, *111*, 12987.
[5] H. Zhang, X. J. Lv, Y. M. Li, Y. Wang, J. H. Li, *ACS Nano* **2010**, *4*, 380.
[6] H. Huang, S. Wang, Y. Zhang, P. K. Chu, *RSC Adv.* **2014**, *4*, 41219.
[7] S. B. Rawal, S. Bera, D. Lee, D. J. Jang, W. I. Lee, *Catal. Sci. Technol.* **2013**, *3*, 1822.
[8] Y. Hu, D. Z. Li, Y. Zheng, W. Chen, Y. H. He, Y. Shao, X. Z. Fu, G. C. Xiao, *Appl. Catal., B* **2011**, *104*, 30.
[9] S. Obregon, G. Colon, *RSC Adv.* **2014**, *4*, 6920.
[10] P. G. Moses, C. G. Van de Walle, *Appl. Phys. Lett.* **2010**, *96*, 021908.
[11] H. L. Lu, M. Yang, Z. Y. Xie, Y. Geng, Y. Zhang, P. F. Wang, Q. Q. Sun, S. J. Ding, D. W. Zhang, *Appl. Phys. Lett.* **2014**, *104*, 161602.
[12] J. Pan, G. Liu, G. M. Lu, H. M. Cheng, *Angew. Chem. Int. Ed.* **2011**, *50*, 2133.
[13] G. Liu, J. C. Yu, G. Q. Lu, H. M. Cheng, *Chem. Commun.* **2011**, *47*, 6763.
[14] Y. Zhang, B. Deng, T. R. Zhang, D. M. Gao, A. W. Xu, *J. Phys. Chem. C* **2010**, *114*, 5073.
[15] L. L. Wang, J. Ge, A. L. Wang, M. S. Deng, X. J. Wang, S. Bai, R. Li, J. Jiang, Q. Zhang, Y. Luo, Y. J. Xiong, *Angew. Chem. Int. Ed.* **2014**, *53*, 5107.
[16] S. Bai, J. Ge, L. L. Wang, M. Gong, M. S. Deng, Q. Kong, L. Song, J. Jiang, Q. Zhang, Y. Luo, Y. Xie, Y. J. Xiong, *Adv. Mater.* **2014**, *26*, 5689.
[17] S. S. Dunkle, R. J. Helmich, K. S. Suslick, *J. Phys. Chem. C* **2009**, *113*, 11980.
[18] A. Kudo, K. Ueda, H. Kato, I. Mikami, *Catal. Lett.* **1998**, *53*, 229.
[19] A. Kudo, K. Omori, H. Kato, *J. Am. Chem. Soc.* **1999**, *121*, 11459.
[20] R. G. Li, F. X. Zhang, D. G. Wang, J. X. Yang, M. R. Li, J. Zhu, X. Zhou, H. X. Han, C. Li, *Nat. Commun.* **2013**, *4*, 1432.
[21] D. E. Wang, H. F. Jiang, X. Zong, Q. A. Xu, Y. Ma, G. L. Li, C. Li, *Chem. Eur. J.* **2011**, *17*, 1275.
[22] C. J. Li, P. Zhang, R. Lv, J. W. Lu, T. Wang, S. P. Wang, H. F. Wang, J. L. Gong, *Small* **2013**, *9*, 3951.
[23] J. J. Sun, X. Y. Li, Q. D. Zhao, J. Ke, D. K. Zhang, *J. Phys. Chem. C* **2014**, *118*, 10113.
[24] Y. Xu, M. A. A. Schoonen, *Am. Mineral.* **2000**, *85*, 543.
[25] M. Jakob, H. Levanon, P. V. Kamat, *Nano Lett.* **2003**, *3*, 353.
[26] M. X. Zhang, P. M. Kelly, M. Qian, J. A. Taylor, *Acta Mater.* **2005**, *53*, 3261.
[27] J. T. Mayer, U. Diebold, T. E. Madey, E. Garfunkel, *J. Electron. Spectrosc. Relat. Phenom.* **1995**, *73*, 1.
[28] H. B. Fu, S. C. Zhang, T. G. Xu, Y. F. Zhu, J. M. Chen, *Environ. Sci. Technol.* **2008**, *42*, 2085.
[29] J. Y. Zhang, W. J. Luo, W. Li, X. Zhao, G. G. Xue, T. Yu, C. F. Hang, M. Xiao, Z. S. Li, Z. G. Zou, *Electrochem. Commun.* **2012**, *22*, 49.
[30] H.-P. Xia, X.-J. Wang, *Appl. Phys. Lett.* **2006**, *89*, 051917.
[31] H. Mizoguchi, H. Kawazoe, H. Hosono, S. Fujitsu, *Solid State Commun.* **1997**, *104*, 705.
[32] D. E. Wang, R. G. Li, J. Zhu, J. Y. Shi, J. F. Han, X. Zong, C. Li, *J. Phys. Chem. C* **2012**, *116*, 5082.
[33] S. Kohtani, J. Hiro, N. Yamamoto, A. Kudo, K. Tokumura, R. Nakagaki, *Catal. Commun.* **2005**, *6*, 185.